

SCIENTIFIC REPORTS



OPEN

A broadband tunable terahertz negative refractive index metamaterial

Fang Ling, Zheqiang Zhong, Renshuai Huang & Bin Zhang

A strategy to greatly broaden negative refractive index (NRI) band, reduce loss and ease bi-anisotropy of NRI metamaterials (MMs) has been proposed at terahertz frequencies. Due to the symmetric structure of the MM, the transmission and refractive index are independent to polarizations of incident radiations, and a broadband NRI is obtainable for the range of the incident angle from 0° to 26° . In addition, THz MMs' properties such as transmission, phase and negative refraction exhibit a real-time response by controlling the temperature. The results indicate that the maximum bands of the negative and double-negative refraction are 1.66 THz and 1.37 THz for the temperature of 40°C and 63°C , respectively. The figure of merit of the MMs exceeds 10 (that is, low loss) as the frequency increases from 2.44 THz to 2.56 THz in the working temperature range, and the maximum figure of merit is 83.77 at 2.01 THz where the refractive index is -2.81 for a given temperature of 40°C . Furthermore, the negative refraction of the MMs at the low loss band is verified by the classical method of the wedge, and the symmetric slab waveguide based on the proposed MM has many unique properties.

Negative index MMs (NIMs) provide numerous unusual properties and phenomena because of their special interaction with incident radiation, which would be applied to some important fields such as superlens¹, slow light device², and communication system etc³. The first theoretical investigation of NIMs was proposed by Veselago in 1968⁴, and experimentally demonstrated until 2001 by Shelby, Smith and Schultz⁵. Further, the basic mechanism of NIMs condition is $\varepsilon_1\mu_2 + \varepsilon_2\mu_1 < 0$ (the permittivity $\varepsilon = \varepsilon_1 + i\varepsilon_2$, the permeability $\mu = \mu_1 + i\mu_2$) instead of both ε_1 and μ_1 being negative simultaneously⁶. Thus, the NIMs of double-negative MMs with simultaneous negative ε_1 and μ_1 and single-negative MMs with single negative ε_1 or μ_1 can be obtained by tailoring the geometry⁷ or configuring the unit structure arrays⁸. The electromagnetic response of the MMs can be dynamically controlled by changing illumination⁹, temperature¹⁰ and voltage etc¹¹, and the controllable characteristics of the MMs are particularly important for manipulating electromagnetic radiation at terahertz (THz) frequencies where the nature material response is somewhat rare.

Multiphoton microfabrication enables the production of three-dimensional (3D) microstructures with sub-100 nm resolution via direct laser writing (DLW) using a femtosecond laser pulsed¹², and lithography of 3D polymeric templates by DLW with feature sizes in less than 100 nm has become routine and is even available commercially¹³. Therefore, combined with atomic-layer deposition and/or chemical vapor deposition (CVD), some 3D bulk MMs have been fabricated, especially at frequencies range from mid-IR to visible^{13–16}. Accordingly, THz MMs based on three-dimensional 3D standing structures have been fabricated and characterized, and unfortunately, due to the strong bi-anisotropy of the structure, the refractive index is always positive despite of the ε_1 and μ_1 presenting negative values^{17,18}. Although the 3D THz NIMs based on standing structure have been achieved, they are sensitive to the polarizations and incident angles, and exhibit a strong bi-anisotropy as well owing to the asymmetric structure^{8,19}. Besides, the 3D THz NIMs composed of stacking up multiple fishnet functional layers indicates high figure of merit (FOM)^{20–22}, but the NRI band with the FOM higher than 10 is narrow, and the ability to control refractive index is low. Therefore, the realization of waveguide and other applications of these 3D THz NIMs are limited because of the strong bi-anisotropy and the low FOM²³.

In this paper, a new structure for THz NIMs with symmetric 3D split-ring resonators (SRRs) has been designed and characterized. The NIMs exhibit properties of thermal tunability, broad-band negative refraction, high FOM, polarization independence and low sensitivity to incident angles between 0° and 26° . The performance of the NIMs is stable between 10°C and 40°C , and the negative refractive properties can be thermally controlled by tuning the

College of Electronics and Information Engineering, Sichuan University, Chengdu, 610065, China. Correspondence and requests for materials should be addressed to B.Z. (email: zhangbinff@sohu.com)

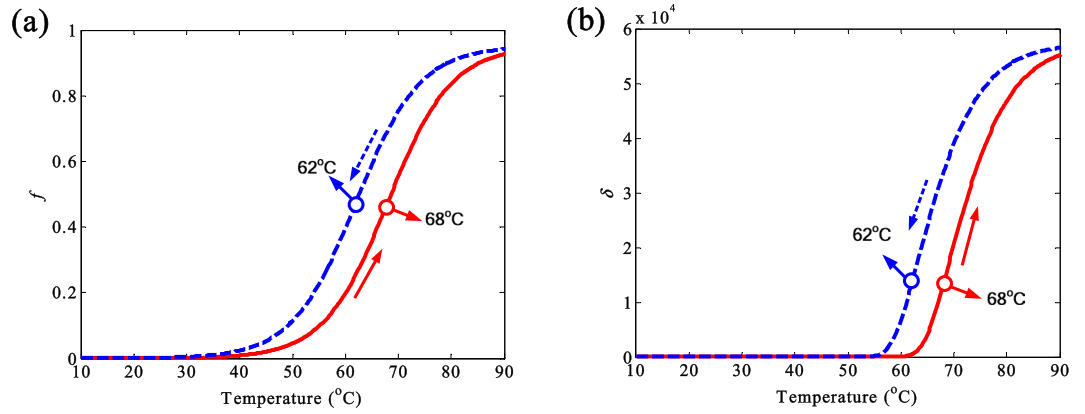


Figure 1. (a) The volume fraction f and (b) the effective conductivity σ of VO₂ at different temperatures for heating ($T_0 = 68^\circ\text{C}$) and cooling ($T_0 = 62^\circ\text{C}$) processes with the hysteresis of $\Delta T = 6^\circ\text{C}$.

temperature from 40 °C to 80 °C. The maximum bandwidths of the NRI and double-negative index are 1.66 THz and 1.37 THz when the temperature is 40 °C and 63 °C, respectively. Additionally, the maximum FOM is 83.77 for a refractive index of -2.81 at 2.01 THz, and the FOM always exceeds 10 when the frequency increases from 2.44 THz to 2.56 THz at the research range of temperature. Finally, the negative refraction of the NIMs is proved by the classical method of wedge, and applications of symmetric parallel waveguide are also discussed in detail.

Results and Discussions

The thermal tunable vanadium dioxide (VO₂) is an ideal material for smart thermal control system due to its reversible phase transition from an insulator to a metallic phase at critical temperature of around 67 °C²⁴, and the phase transition time is on a scale of 10 ns by heating²⁵, as well as its effective conductivity. Another important feature is that VO₂ is highly transparent for electromagnetic wave below 6.7 THz²⁶. The dielectric function ϵ_m of metallic phase follows the Drude²⁷, i.e.

$$\epsilon_m(\omega) = \epsilon_\infty - \frac{\omega_p^2}{\omega^2 + i\omega/\tau} \tag{1}$$

where the $\epsilon_\infty = 9$ represents the high-frequency permittivity; ω denotes angular frequency of THz radiation. $\tau = m^* \mu / e$ is the relaxation time, the $m^* = 2m_e$ represents the effective mass, and the carrier mobility is $\mu = 2 \text{ cm}^2 / (\text{V}\cdot\text{s})$. The plasma frequency is $\omega_p = (Ne^2/(\epsilon_0 m^*))^{-1/2}$, the effective mass carrier density is $N = 8.7 \times 10^{21} \text{ cm}^{-3}$, m_e and e represent the mass of free electron and electronic charge, respectively. The effective dielectric function of VO₂ film in the process of insulator-metal transition can be well described by the Bruggeman effective medium theory (EMT)²⁸:

$$\epsilon_{\text{eff}} = \frac{1}{4} \left\{ \epsilon_i(2 - 3f) + \epsilon_m(3f - 1) + \sqrt{[\epsilon_i(2 - 3f) + \epsilon_m(3f - 1)]^2 + 8\epsilon_i\epsilon_m} \right\} \tag{2}$$

where ϵ_i is insulating permittivity, and $\epsilon_i = \epsilon_\infty = 9$. The volume fraction f of conductive regions is given by²⁸:

$$f(T) = f_{\text{max}} \left\{ 1 - \frac{1}{1 + \exp[(T - T_0)/\Delta T]} \right\} \tag{3}$$

where T_0 denotes the transmission temperature of VO₂ (the heating transmission temperature $T_0 = 68^\circ\text{C}$, the cooling transmission temperature $T_0 = 62^\circ\text{C}$); the hysteresis is $\Delta T = 6^\circ\text{C}$; the volume fraction f_{max} of metallic domain is 0.95. The effective conductivity σ of the metallic phase VO₂ can be described as²⁹:

$$\sigma = i\epsilon_0\omega(1 - \epsilon_{\text{eff}}) \tag{4}$$

where ϵ_0 labels vacuum permittivity. According to the Eqs (1–4), the thermal properties of the VO₂ can be simulated, as given in Fig. 1.

It is clear that the volume fraction f and the effective conductivity σ of VO₂ varying with the temperature show thermal tunability and a typical hysteresis behavior. During the heating process, f remains below 1% (i.e., the metallic property of VO₂ can be ignored) at the temperature between 10 °C and 40 °C. Although f increases obviously with the temperature raising from 40 °C to 60 °C, the effective conductivity σ is below 100 S/m. When the temperature rises from 61 °C to 80 °C, σ increases abruptly from 173.5 S/m to $4.673 \times 10^4 \text{ S/m}$ due to the metallic phase transition at 68 °C. If the temperature exceeds 80 °C, σ stabilizes gradually. Similarly, σ represents thermal tunability as well for the cooling process, while the critical temperature changes to 62 °C. Accordingly, the THz thermal tunable 3D NIMs composed of quad-vertical metallic SRRs and thermo-sensitive VO₂ films integrated in the substrate has been proposed. In order to enhance the magnetic response and ease bi-anisotropy of the MM, the symmetric metal slices on the front and bottom surfaces of the dielectric substrate are connected via metal cylinders.

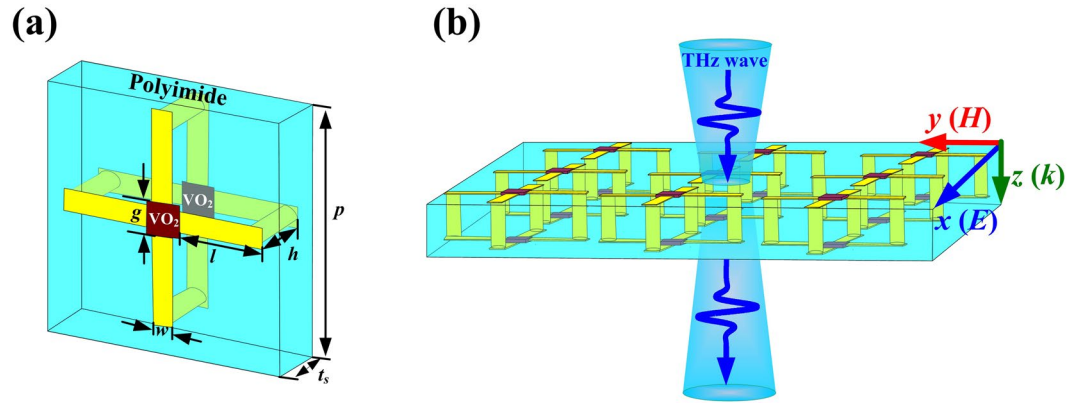


Figure 2. Schematic of the broadband THz NIMs. (a) Typical dimensions for unit cell of the SRRs. (b) Perspective view of the NIMs array at the normally incident THz wave.

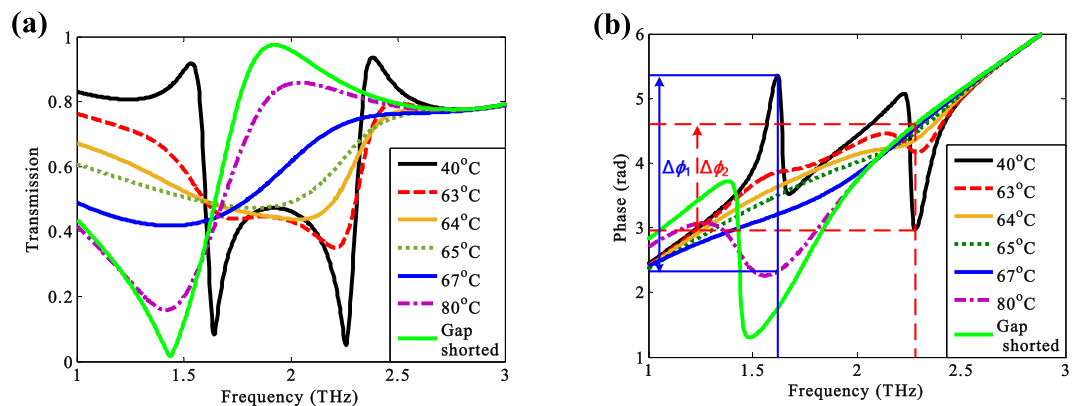


Figure 3. (a) The normalized transmission spectra and (b) transmission phase spectra at different temperatures. The green-solid curves correspond to the gaps shorted with copper. The blue-solid and red-dashed lines of (b) indicate the phase shifts at 1.62 THz and 2.28 THz, respectively.

Figure 2 details the structure of the THz NIMs with the lateral dimension $p = 70 \mu\text{m}$, and the length (l) and the width (w) of the SRRs are $25 \mu\text{m}$ and $6 \mu\text{m}$, respectively. The thicknesses of the metallic portions, VO₂ films and dielectric spacer are $t_c = 0.2 \mu\text{m}$, $t_v = 0.5 \mu\text{m}$ and $t_s = 18 \mu\text{m}$, respectively. The heights of the vertical cylinder (h) are same as t_s , and the radius of the vertical cylinder (r) and the gaps of the SRRs (g) are $3 \mu\text{m}$ and $10 \mu\text{m}$, respectively. Generally, the geometries of VO₂ films with less than $10 \mu\text{m}$ can be shaped by lithography and etching³⁰, and there are many the hybrid structures composed of metallic resonators and VO₂ films have been fabricated and reported^{31–33}. Commonly, the first fabrication step of these hybrid structures is shaping the VO₂ film by combing the lithography and etching technology, and the second step is fabricating the metallic resonators. Therefore, the THz 3D structure composed of metallic resonators and square VO₂ film with length $10 \mu\text{m} \times 10 \mu\text{m}$ and gap width $60 \mu\text{m} \times 60 \mu\text{m}$ can be fabricated as well. The first step is shaping the square VO₂ films by lithography and etching^{30–33}, and the second step is fabricating the inherent connective cylinders by DLW and CVD^{13–16,34,35}.

The transmission of the THz NIMs is calculated by the commercial program CST Microwave Studio 2014 with the frequency domain solver. The propagation wave vector (\mathbf{k}) is perpendicular to the NIMs whereas the electric field (\mathbf{E}) and magnetic field (\mathbf{H}) are parallel to the incident plane (floquet ports are set along the z direction, and unit-cell boundaries are applied to the x and y directions). The tetrahedral meshes with the adaptive meshing method are employed. The lossy copper with a frequency-independent conductivity $\sigma = 5.8 \times 10^7 \text{ S/m}$ ³⁶ and the lossy polyimide with a relative permittivity $\epsilon_r = 3.5$ ³⁷ are chosen as the metallic pattern and the dielectric spacer to accurately calculate the 3D MMs, respectively.

The normalized transmission and phase spectra of the THz NIMs at different temperatures are plotted in Fig. 3. The performance of the NIMs is stable with the temperature increasing from 10°C to 40°C due to the almost unchanged conductivity of the VO₂ films [see the Fig. 1]. As given in Fig. 3(a), there are two resonance frequencies at 1.64 THz and 2.23 THz for a given temperature of 40°C . With the temperature increasing from 40°C to 63°C , the lower resonance frequency presents blue-shift, while the higher resonance frequency exhibits red-shift. The lower resonance frequency disappears, and the higher resonance frequency decreases continuously when the temperature increases to 64°C . The resonance frequency redshifts to 1.83 THz with the temperature increasing to 65°C . As the temperature reaches to 67°C , the resonance frequency further shifts to 1.42 THz with a transmission of 41.79%. Further, the transmission dip located at 1.42 THz decreases to 15.96% when the

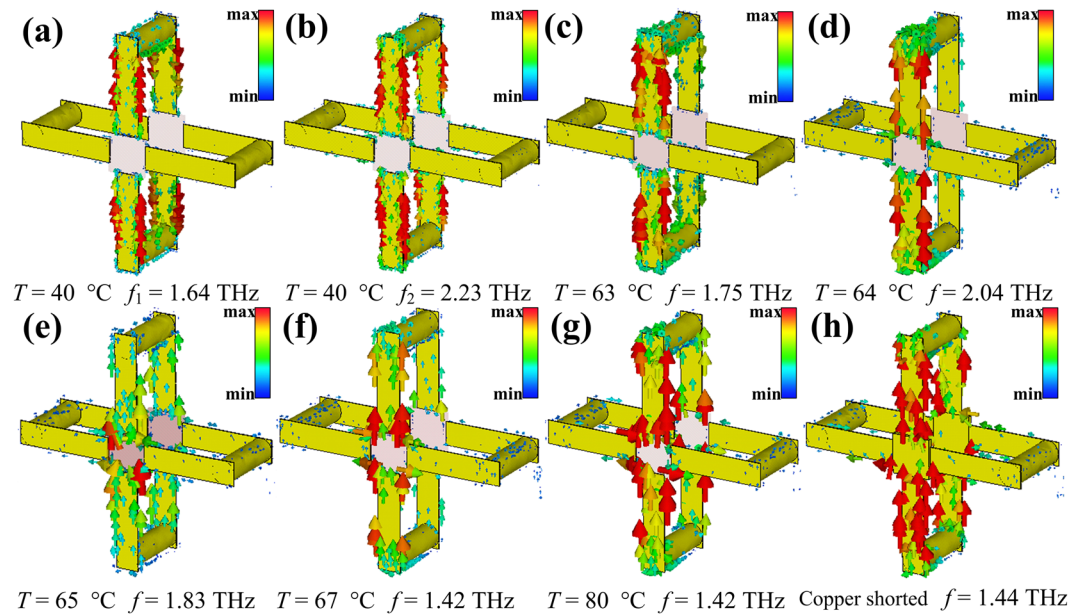


Figure 4. The surface current distributions of the SRRs normally incident by THz radiation for a given temperature and resonance frequency.

temperature increases to 80 °C. The gaps are totally shortened by copper, and therefore, the transmission dip locates at 1.44 THz with a transmission dip of 1.59% owing to the conductivity of copper higher than that of the VO₂ films.

Another functionality of the THz NIMs manipulated by temperature is phase shifting. As the blue-solid vertical line indicated in Fig. 3(b), the phases of the THz transmission are $\phi_{40} = 5.35$ rad and $\phi_{80} = 2.33$ rad at 1.62 THz, and the corresponding phase shift is $\Delta\phi_1 = 0.96\pi$. Meanwhile, indicated by the red-dashed vertical line, the phases of the THz transmission are $\phi_{40} = 2.79$ rad and $\phi_{80} = 4.60$ rad, resulting in a phase shift of $\Delta\phi_2 = -0.58\pi$ at 2.28 THz. Hence, the designed NIMs can function as a THz double-phase shifter. In order to study and understand the dynamic coupling effect of the NIMs for different temperatures, the distributions of the surface current at different resonance frequencies are calculated.

Figure 4(a,b) presents the surface current distributions of the SRRs corresponding to the two resonance frequencies for a given temperature $T = 40$ °C. At the lower resonance frequency ($f_1 = 1.64$ THz), the circulating current causes a lot of charges accumulation on both gaps forming an inductive–capacitive (LC) resonance, which can be considered as a magnetic dipole described by Lorentz model³⁸. At the higher resonance frequency ($f_2 = 2.23$ THz), the surface current exhibits symmetric parallel loops on the top and bottom arms, which gives rise to a strong scattering leading to a broad dipole resonance feature³⁹. It can be seen in Fig. 4(c) that the density of the surface current decreases with the temperature rising to 63 °C, which leads to the attenuation of the LC resonance. From Fig. 4(d) we can see that the surface current at 2.04 THz focuses on the top arm of the SRRs for the case of temperature $T = 64$ °C. Therefore, the LC resonance disappears, and the gaps of the SRRs are effectively shorted by VO₂ films.

In Fig. 4(e), the symmetric parallel current distribution is observed. Figure 4(e–g) depicts that the resonance is gradually strengthened with the increasing temperature from 65 °C to 80 °C. For the case of the gaps shorted by copper, the density of the surface current increases further, as illustrated in Fig. 4(h). Consequently, the reasons why the blueshift of the LC resonance frequency and the redshift of the dipole resonance frequency can be regarded as the decreasing effective C and the increasing effective L ($f_{\text{resonance}} \propto 1/(LC)^{-1/2}$)^{40,41}, respectively. In order to study the characteristics of the NIMs, Fig. 5 gives the retrieved constitutive parameters of the NIMs at different temperatures.

Because the scale of the unit cell of the NIMs is smaller than the operating wavelength and the structure is symmetric along the THz propagation, i.e. $S_{11} = S_{22}$, the standard retrieval method is performed to extract the effective ε and μ ⁴². The figure of merit (FOM, $\text{FOM} = |\text{Re}(n)/\text{Im}(n)|$) is a well-established measure of the strength of the NRI with respect to the losses^{20,43,44}. Figure 5 shows the retrieval parameters and FOM as a function of frequency at the normal incident angle with different temperatures, in which the green and blue regions reveal the ranges of single-negative refraction with positive μ_1 and ε_1 , respectively. In Fig. 5(a), there is a broadband of negative refraction that lies between 1.27 THz and 2.93 THz when the temperature is $T = 40$ °C, and the broadband is composed of four single-negative and three double-negative bands which are highlighted by the green and blue areas, respectively. Additionally, the FOM in double-negative region is greater than that in single negative regions, and the maximum value of FOM is 83.77 at 2.01 THz (where $\text{Re}(n)$ is -2.81). For the case of $T = 63$ °C shown in Fig. 5(b), the maximum bandwidth of the double-negative refraction is obtained, which lies between 1.35 THz and 2.72 THz. However, the FOM in the double-negative refraction region decreases with the weakening resonance.

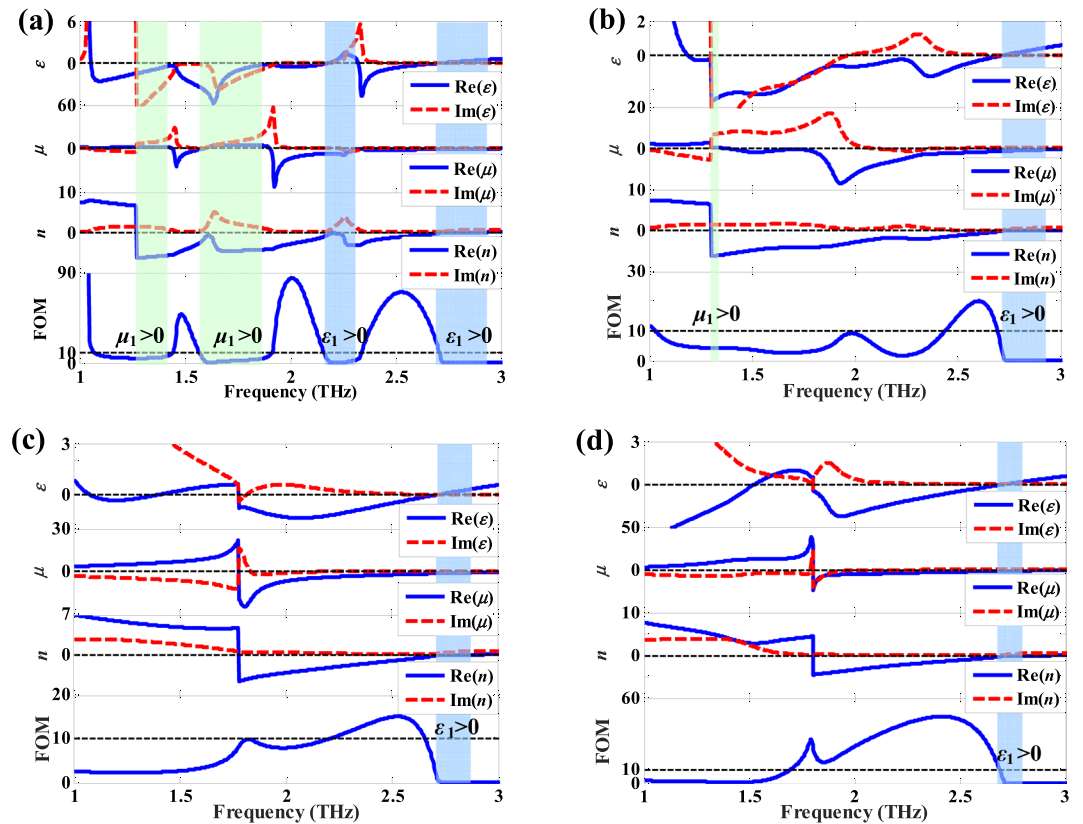


Figure 5. The retrieved parameters of the NIMs for a given temperature (a) 40 °C, (b) 63 °C, (c) 67 °C and (d) 80 °C, respectively. The green and blue regions mark the ranges of single-negative index with $\epsilon_1 > 0$ and $\mu_1 > 0$, respectively.

For the cases of $T = 67^\circ\text{C}$ and $T = 80^\circ\text{C}$ depicted in Fig. 5(c,d), the negative-refractive band of the NIMs only has a single-negative refraction band with $\epsilon_1 > 0$ at the higher frequency. The FOM of the double-negative refraction increases with the increasing temperature from 63 °C to 80 °C, because the resonance of the NIMs is gradually enhanced with the increasing conductivity of the VO₂ films. Consequently, the tunable NRI is achieved, and the maximum bandwidths of the NRI and double NRI are 1.66 THz and 1.37 THz for the temperature of 40 °C and 63 °C, respectively. The FOM of the double-negative band between 2.44 THz and 2.56 THz is always higher than 10 (that is, low loss) when the temperature increases from 40 °C to 80 °C.

In practical applications such as THz waveguide, the independence of polarization and incident angles is desirable. Hence, the impacts of polarization and incident angles on the transmission and refraction also are shown in Fig. 6.

Due to the symmetrical characteristic of the NIMs, the normalized transmission and the real part of the refractive index of the NIMs are independent of polarization angles under the normally incident THz radiation for the case of temperature $T = 40^\circ\text{C}$, as given in Fig. 6(a). From Fig. 6(b) we can see that the transmission and the real part of the refractive index of the NIMs have low sensitivity to the incident angles between 0° and 26° , whereas a positive refractive index band appears in the NRI band at 27° . The transmission and refraction at the low frequency change slightly with the increasing incident angle, but change drastically at high frequency. In order to further study the electromagnetic response of the NIMs at different incident angles, Fig. 6(c) gives the real parts of ϵ_1 and μ_1 of the NIMs at different incident angles. The positive refractive index band is induced by the magnetic response instead of the electric response at 27° . Consequently, a tunable THz NIMs with the properties such as thermo tunability, polarization independence, less incident sensitivity and high FOM is realized.

A popular and useful way to demonstrate the negative refraction is to calculate a wedge³⁸. The wedge samples of the NIMs are composed of 6×6 unit cells in both x and z directions with one-unit-cell stairs. The adjacent unit cells are contact in x direction, and one unit cell is considered in y direction because the MMs in x and y directions are symmetric and periodic. Thus, it is not necessary to construct the negative refractive behavior in y direction. Besides, in order to avoid the interference between the adjacent unit cells in propagation direction (z direction), the adjacent samples are separated by vacuum with thickness of $2\ \mu\text{m}$. Since the periodicities along the x and z directions are $p_x = 70\ \mu\text{m}$ and $p_z = 19.4\ \mu\text{m}$, the incident angle is determined as $\theta_i = \arctan(p_z/p_x) \approx 15.49^\circ$.

Figure 7 plots the electric field distributions of the wedge at 2.48 THz and 2.51 THz in the y plane for a given temperature $T = 40^\circ\text{C}$. According to the wave fronts indicated by localized field with the strong intensity, the refracted angles θ_r of the wedge sample are about 21.5° and 19.0° at 2.48 THz and 2.51 THz, respectively. By utilizing the Snell's law $n = \sin \theta_r / \sin \theta_i$, the real parts of the refractive indexes $\text{Re}(n)$ of the NIMs at 2.48 THz and 2.51 THz are estimated as -1.40 and -1.22 , respectively. The retrieval $\text{Re}(n)$ of the NIMs at 2.48 THz and

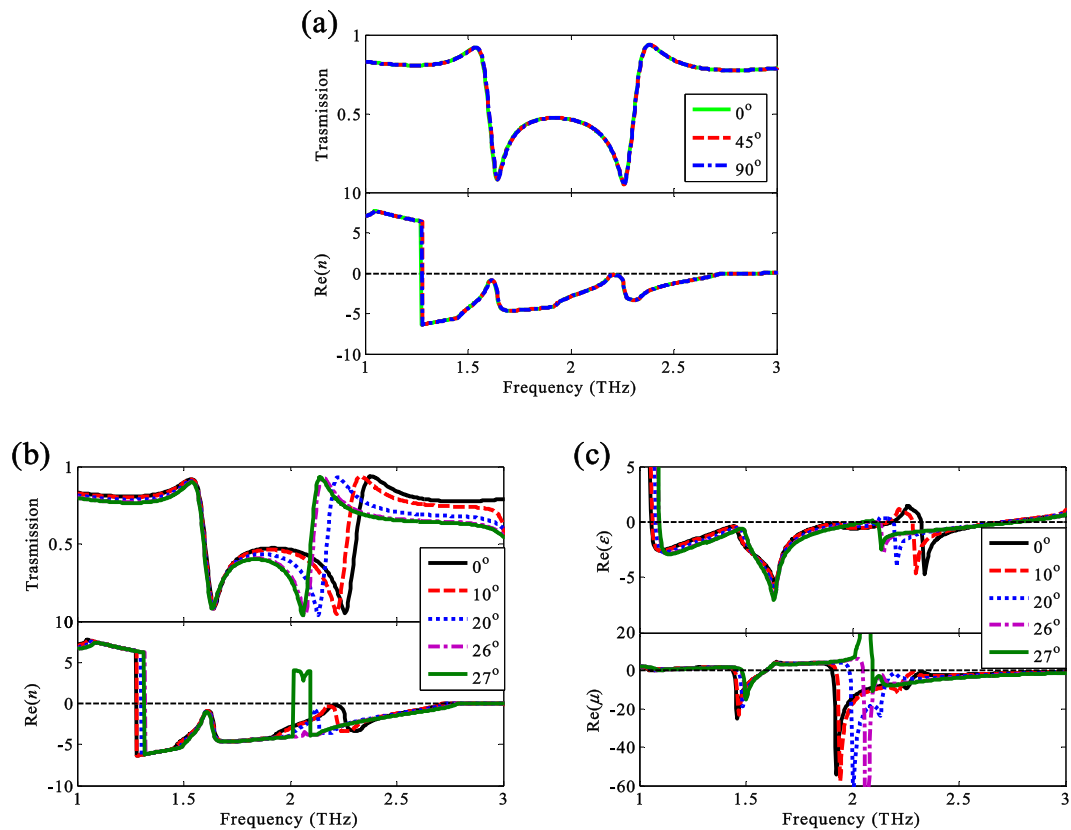


Figure 6. The normalized transmission spectra and refractive index of the NIMs (a) at different polarization angles and (b) different incident angles for a given temperature $T = 40^\circ\text{C}$. (c) The real parts of the permittivity and permeability of the NIMs at different incident angles when the temperature is $T = 40^\circ\text{C}$.

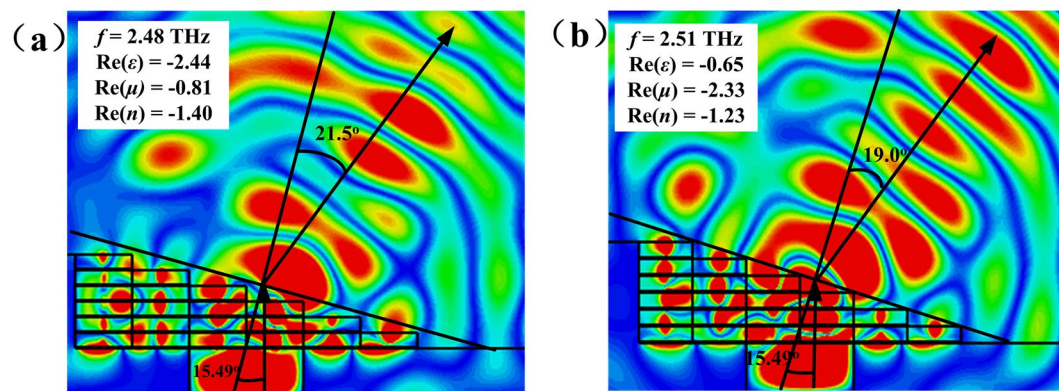


Figure 7. The electric field distributions of the refracted THz radiation at (a) 2.48 THz and (b) 2.51 THz for the NIMs at 40°C .

2.51 THz are -1.40 and -1.23 , which indicates that the retrieval values of the $\text{Re}(n)$ are consistent with that estimated by the Snell's law of the wedge.

The waveguide composed of high FOM NIMs, which is an important device of the THz transmission system, has many unique properties⁴⁵ such as lack of fundamental mode and cutoff frequency. Accordingly, the thermally controlled NIMs at the low loss band can be applied to the symmetric slab waveguide. The k_{1x} and k_{2x} are the transverse wave numbers in free space and NIMs along the x direction, respectively, and can be written as^{45,46}:

$$k_{1x}^2 = \beta^2 - \frac{\omega^2}{c^2} \epsilon_1 \mu_1 \tag{5}$$

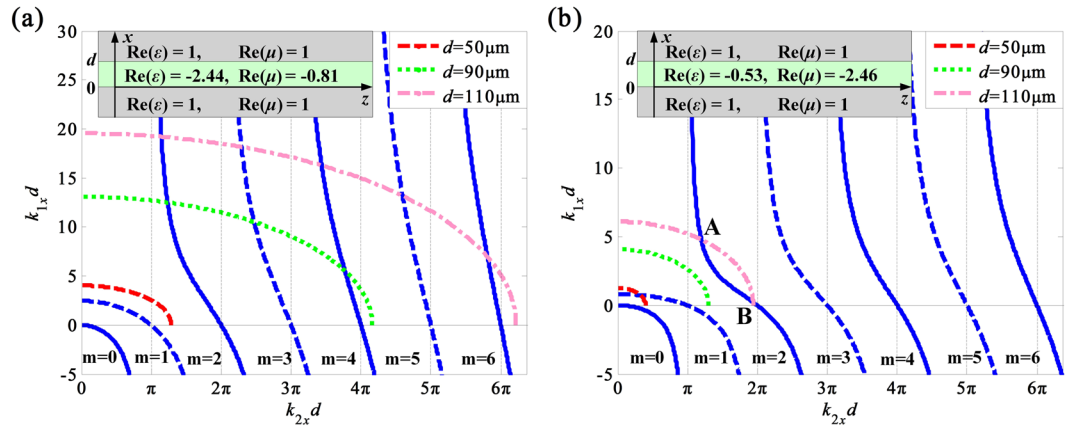


Figure 8. The TE guided modes of the NIMs symmetric slab waveguide with different thicknesses at 2.48 THz for the given temperatures of (a) 40 °C and (b) 80 °C. The insets of (a) and (b) are the schematics of the NIMs waveguide geometries, and the z direction is chosen as the direction of propagation of guided modes. The A and B points in (b) represent that there are two different intersections.

$$k_{2x}^2 = \frac{\omega^2}{c^2} \epsilon_2 \mu_2 - \beta^2 \tag{6}$$

where $\text{Re}(\beta)$ is the THz wave transmission constant, the ω is the angular frequency of the incident field. The guidance condition of the homogeneous NIMs symmetric slab waveguide can be written as:

$$k_1 d = \frac{\mu_1}{\mu_2} k_{2x} d \cdot \tan\left(\frac{k_{2x} d}{2} - \frac{m\pi}{2}\right) \tag{7}$$

therefore, for even m , the guidance condition can be described as:

$$k_{1x} d = \frac{\mu_1}{\mu_2} k_{2x} d \cdot \tan\left(\frac{k_{2x} d}{2}\right) \tag{8}$$

for the odd m mode, Eq. (7) yields

$$k_{1x} d = -\frac{\mu_1}{\mu_2} k_{2x} d \cdot \cot\left(\frac{k_{2x} d}{2}\right) \tag{9}$$

according to the dispersion relations between the different regions:

$$\begin{cases} (k_z d)^2 - (k_{1x} d)^2 = (k_1 d)^2 \\ (k_z d)^2 + (k_{2x} d)^2 = (k_2 d)^2. \end{cases} \tag{10}$$

The circle function $\rho = (k_{1x} d)^2 + (k_{2x} d)^2$ can be defined according to the electromagnetic parameters of media 1 and 2. In Eq. (10), k_z denotes the transverse wave number in z direction, k_1 and k_2 are the transverse wave numbers in free space and NIMs, respectively. Thus, the transcendental Eqs (8, 9) can be solved by the graphical method. Accordingly, Fig. 8 depicts that the transverse electric (TE) guided modes of the symmetric slab waveguides with different thicknesses d are calculated for a given temperature of 40 °C and 80 °C at 2.48 THz, respectively.

The schematics of the NIMs symmetric slab waveguides with different parameters of NIMs in free space are given in the insets of Fig. 8, and the gray and green areas indicate the free space and NIMs, respectively. The solid-blue curves present the even mode with different m , and dashed-blue curves are odd mode with different m , respectively. The red-dashed, green-dotted and pink-dashed-dotted curves are $\rho = (k_{1x} d)^2 + (k_{2x} d)^2$ with different values d . The intersections of the curves indicate the existence of solutions for guided modes⁴⁵. It can be seen that the NIMs slab waveguide do not support any TE wave at 40 °C, while the TE₁ mode is supported at 80 °C when d is 50 μm. For $d = 90$ μm, the NIMs slab wave guide supports TE₂, TE₃ and TE₄ modes simultaneously for a given temperature of 40 °C, whereas the NIMs waveguide do not support any TE wave at 80 °C. If d increases to 110 μm, the TE₂, TE₃, TE₄, TE₅ and TE₆ modes are supported for the temperature of 40 °C. Besides, there are two modes co-existing for the TE₂ mode, as A and B points represented in Fig. 8(b), which is an unique performance of NIMs waveguide.

Consequently, the performance of the NIMs waveguide can be dynamically tuned by controlling temperature between 40 °C and 80 °C at the low loss frequency band. Moreover, the NIMs has many unique properties different from the conventional slab waveguide: firstly, there is no fundamental guided mode (that is, TE₀ mode) no matter what the value of d is, because the transvers wave number k_{1x} is negative, while the ρ is always positive⁴⁵.

Secondly, for $m = 1$, the transvers wave number $k_{1x}d$ is a determined value for $k_{2x}d = 0$, and $k_{1x}d$ is 0 for $k_{2x}d = \pi$, as described in Eq. (9) and Fig. 8. Therefore, the lowest mode TE_1 of the NIMs waveguide cannot be arbitrary value from 0 to $+\infty$ (that is, the TE_1 mode has cutoff frequency), while the lowest mode of the conventional slab waveguide has no cutoff frequency. In addition, the two modes may be co-existing for a mode, as A and B intersection illustrated in Fig. 8(b).

Conclusion

A THz NIMs composed of symmetric SRRs and thermo-sensitive VO_2 films has been proposed. The transmission, phase and refractive index of the proposed NIMs are dynamically tunable with the increasing temperature from 40 °C to 80 °C. Due to the symmetric structure of the NIMs, the transmission and refractive index are independent to the polarizations of the incident THz radiation, and exhibits low sensitivity to the incident angles between 0° to 26°. When the frequency rises from 2.44 THz to 2.56 THz, the FOMs always exceed 10, and its peak value is 83.77 for the case of $f = 2.01$ THz, $T = 40$ °C. The negative refractive characteristics of the NIMs at 2.48 THz and 2.51 THz are verified by the classical method of the wedge, which coincides with the retrieval values of the NRI. Besides, the NIMs symmetric slab waveguide has many unique properties such as lack of fundamental mode, cutoff frequency and co-existing of two modes. The properties of the NIMs slab waveguide are dynamically tunable by controlling the temperature from 40 °C to 80 °C, whereas they are in steady-state when the temperature increases from 10 °C to 40 °C.

References

- Pendry, J. B. Negative refraction makes a perfect lens. *Phys. Rev. Lett.* **85**, 3966 (2000).
- Wu, C., Khanikaev, A. B. & Shvets, G. Broadband slow light metamaterial based on a double-continuum Fano resonance. *Phys. Rev. Lett.* **106**, 107403 (2011).
- Nguyen, H. M. Negative index materials and their applications: recent mathematics progress. *Chinese Ann. Math. B* **38**, 601–628 (2017).
- Veselago, V. G. The electrodynamics of substances with simultaneously negative values of ϵ and μ . *Sov. Phys. Usp.* **10**, 509 (1968).
- Shelby, R. A., Smith, D. R. & Schultz, S. Experimental verification of a negative index of refraction. *Science* **292**, 77–79 (2001).
- Tung, N. T. *et al.* Single- and double-negative refractive indices of combined metamaterial structure. *J. Appl. Phys.* **106**, 053109 (2009).
- Chen, H. *et al.* Left-handed materials composed of only S-shaped resonators. *Phys. Rev. E* **70**, 057605 (2004).
- Meng, Q., Zhong, Z. & Zhang, B. Hybrid three-dimensional dual- and broadband optically tunable terahertz metamaterials. *Sci. Rep.* **7**, 45708 (2017).
- Chen, H. T. *et al.* Active terahertz metamaterial devices. *Nature* **444**, 597–600 (2006).
- Lv, T. T. *et al.* Hybrid metamaterial switching for manipulating chirality based on VO_2 phase transition. *Sci. Rep.* **6**, 23186 (2016).
- Deng, G., Xia, T., Yang, J., Qiu, L. & Yin, Z. Tunable terahertz metamaterial with a graphene reflector. *Mater. Res. Express* **3**, 115801 (2016).
- Maruo, S. & Fourkas, J. T. Recent progress in multiphoton microfabrication. *Laser Photonics Rev.* **2**, 100–111 (2008).
- Rill, M. S. *et al.* Photonic metamaterials by direct laser writing and silver chemical vapour deposition. *Nat. Mater.* **7**, 543 (2008).
- Gansel, J. K. *et al.* Gold helix photonic metamaterial as broadband circular polarizer. *Science* **325**, 1513–1515 (2009).
- Freymann, G. V. *et al.* Three-dimensional nanostructures for photonics. *Adv. Funct. Mater.* **20**, 1038–1052 (2010).
- Güney, D. Ö., Koschny, T., Kafesaki, M. & Soukoulis, C. M. Connected bulk negative index photonic metamaterials. *Opt. Lett.* **34**, 506–508 (2009).
- Fan, K., Strikwerda, A. C., Tao, H., Zhang, X. & Averitt, R. D. Stand-up magnetic metamaterials at terahertz frequencies. *Opt. Express* **19**, 12619–12627 (2011).
- Fan, K., Strikwerda, A. C., Zhang, X. & Averitt, R. D. Three-dimensional broadband tunable terahertz metamaterials. *Phys. Rev. B* **87**, 161104 (2013).
- Zhang, S. *et al.* Negative refractive index in chiral metamaterials. *Phys. Rev. Lett.* **102**, 023901 (2009).
- Paul, O., Imhof, C., Reinhard, B., Zengerle, R. & Beigang, R. Negative index bulk metamaterial at terahertz frequencies. *Opt. Express* **16**, 6736–6744 (2008).
- Valentine, J. *et al.* Three-dimensional optical metamaterial with a negative refractive index. *Nature* **455**, 376–379 (2008).
- Wu, D. *et al.* Broadband mid-infrared dual-band double-negative metamaterial: realized using a simple geometry. *Plasmonics*, 1–9 (2017).
- Weis, P., Paul, O., Imhof, C., Beigang, R. & Rahm, M. Strongly birefringent metamaterials as negative index terahertz wave plates. *Appl. Phys. Lett.* **95**, 171104 (2009).
- Fan, F., Hou, Y., Jiang, Z. W., Wang, X. H. & Chang, S. J. Terahertz modulator based on insulator–metal transition in photonic crystal waveguide. *Appl. Optics* **51**, 4589–4596 (2012).
- Briggs, R. M., Pryce, I. M. & Atwater, H. A. Compact silicon photonic waveguide modulator based on the vanadium dioxide metal-insulator phase transition. *Opt. Express* **18**, 11192–11201 (2010).
- Chen, C. *et al.* VO_2 multidomain heteroepitaxial growth and terahertz transmission modulation. *Appl. Phys. Lett.* **97**, 211905 (2010).
- Mandal, P., Speck, A., Ko, C. & Ramanathan, S. Terahertz spectroscopy studies on epitaxial vanadium dioxide thin films across the metal-insulator transition. *Opt. Lett.* **36**, 1927–1929 (2011).
- Jepsen, P. U. *et al.* Metal-insulator phase transition in a VO_2 thin film observed with terahertz spectroscopy. *Phys. Rev. B* **74**, 205103 (2006).
- Walther, M. *et al.* Terahertz conductivity of thin gold films at the metal-insulator percolation transition. *Phys. Rev. B* **76**, 125408 (2007).
- Sun K, *et al.* VO_2 thermo-chromic metamaterial-based smart optical solar reflector. *ACS Photonics* (2018).
- Huitema, L., Crunteanu, A., Wong, H. & Arnaud, E. Highly integrated VO_2 -based tunable antenna for millimeter-wave applications. *Appl. Phys. Lett.* **110**, 203501 (2017).
- Zhu, Y. *et al.* Tunable dual-band terahertz metamaterial bandpass filters. *Opt. Lett.* **38**, 2382–2384 (2013).
- Crunteanu, A. *et al.* Tunable THz metamaterials based on phase-changed materials (VO_2) triggered by thermal and electrical stimuli. *Proc. SPIE* **10103**, 101031H-1–8 (2017).
- Deubel, M. *et al.* Direct laser writing of three-dimensional photonic-crystal templates for telecommunications. *Nat. Mater.* **3**, 444 (2004).
- Zhang, X., Debnath, S. & Güney, D. Ö. Hyperbolic metamaterial feasible for fabrication with direct laser writing processes. *J. Opt. Soc. Am. B* **32**, 1013–1021 (2015).
- Yen, T. J. *et al.* Terahertz magnetic response from artificial materials. *Science* **303**, 1494–1496 (2004).

37. Junlin, W., Binzhen, Z., Xin, W. & Junping, D. Flexible dual-band band-stop metamaterials filter for the terahertz region. *Opt. Mater. Express* **7**, 1656–1665 (2017).
38. Wang, J. *et al.* Normal-incidence left-handed metamaterials based on symmetrically connected split-ring resonators. *Phys. Rev. E* **81**, 036601 (2010).
39. Singh, R. *et al.* Observing metamaterial induced transparency in individual Fano resonators with broken symmetry. *Appl. Phys. Lett.* **99**, 201107 (2011).
40. Wang, W., Yan, F., Tan, S., Zhou, H. & Hou, Y. Ultrasensitive terahertz metamaterial sensor based on vertical split ring resonators. *Photonics Res.* **5**, 571–577 (2017).
41. Zhou, J., Zhang, L., Tuttle, G., Koschny, T. & Soukoulis, C. M. Negative index materials using simple short wire pairs. *Phys. Rev. B* **73**, 041101 (2006).
42. Smith, D. R., Vier, D. C., Koschny, T. & Soukoulis, C. M. Electromagnetic parameter retrieval from inhomogeneous metamaterials. *Phys. Rev. E* **71**, 036617 (2005).
43. Shalaev, V. M. Optical negative-index metamaterials. *Nat. Photonics* **1**, 41–48 (2007).
44. Hoffman, A. J. *et al.* Negative refraction in semiconductor metamaterials. *Nat. Mater.* **6**, 946–950 (2007).
45. Shadrivov, I. V., Sukhorukov, A. A. & Kivshar, Y. S. Guided modes in negative-refractive-index waveguides. *Phys. Rev. E* **67**, 057602 (2003).
46. Wu, B. I., Grzegorzczak, T. M., Zhang, Y. & Kong, J. A. Guided modes with imaginary transverse wave number in a slab waveguide with negative permittivity and permeability. *J. Appl. Phys.* **93**, 9386–9388 (2003).

Acknowledgements

This work was supported by China Innovative Talent Promotion Plans for Innovation Team in Priority Fields (Grant No. 2014RA4051) and the Fund of Tianjin Key Laboratory of Optical Thin Film (Grant No. kjwx170620).

Author Contributions

Fang Ling conceived the idea, simulated the sample and calculated the data. Fang Ling, Bin Zhang and Zheqiang Zhong co-wrote the paper. All authors discussed the results and commented on the manuscript, and contributed to the revision of the manuscript and supplementary information.

Additional Information

Competing Interests: The authors declare no competing interests.

Publisher's note: Springer Nature remains neutral with regard to jurisdictional claims in published maps and institutional affiliations.



Open Access This article is licensed under a Creative Commons Attribution 4.0 International License, which permits use, sharing, adaptation, distribution and reproduction in any medium or format, as long as you give appropriate credit to the original author(s) and the source, provide a link to the Creative Commons license, and indicate if changes were made. The images or other third party material in this article are included in the article's Creative Commons license, unless indicated otherwise in a credit line to the material. If material is not included in the article's Creative Commons license and your intended use is not permitted by statutory regulation or exceeds the permitted use, you will need to obtain permission directly from the copyright holder. To view a copy of this license, visit <http://creativecommons.org/licenses/by/4.0/>.

© The Author(s) 2018